



Article

An Effective Charging Torque Elimination Method for Dual-Channel Electric-Drive-Reconstructed Onboard Chargers

Xunhui Cheng , Feng Yu * and Linhao Qiu

School of Electrical Engineering and Automation, Nantong University, Nantong 226019, China; cheng@stmail.ntu.edu.cn (X.C.); 2312320020@stmail.ntu.edu.cn (L.Q.)

* Correspondence: yufeng628@ntu.edu.cn; Tel.: +86-13776929955

Abstract: The idea of electric-drive-reconstructed onboard charger (EDROC) systems, along with the concept of dual-channel charging, offers a novel design, thought to enhance the integration and fault tolerance of the charging system of electric vehicles (EVs). This article investigates a dual-channel EDROC incorporating an asymmetrical six-phase permanent magnet synchronous machine (ASPMSM). A unique operation mode, called the unbalanced charging voltage operation mode, exists in this topology, in case the voltages of the two batteries are unequal. This unbalance results in different winding currents following through two channels, leading to an undesired charging torque in the machine. To ensure the safety of the system, an effective charging torque elimination method, based on dual-channel winding current balance, is proposed, which achieves a dot-shaped current path of torque generation-associated subspace (i.e., α - β subspace) by balancing the dual-channel charging power. Eventually, a controller is designed for the system and a prototype is created, to validate the effectiveness of the proposed method.

Keywords: electric-drive-reconstructed onboard charger (EDROC); dual-channel; electric vehicles (EVs); asymmetrical six-phase permanent magnet synchronous machine (ASPMSM); unbalanced charging voltage operation mode; effective charging torque elimination



Citation: Cheng, X.; Yu, F.; Qiu, L. An Effective Charging Torque Elimination Method for Dual-Channel Electric-Drive-Reconstructed Onboard Chargers. *World Electr. Veh. J.* **2024**, *15*, 205. <https://doi.org/10.3390/wevj15050205>

Academic Editor: Joeri Van Mierlo

Received: 9 April 2024

Revised: 30 April 2024

Accepted: 7 May 2024

Published: 8 May 2024



Copyright: © 2024 by the authors. Licensee MDPI, Basel, Switzerland. This article is an open access article distributed under the terms and conditions of the Creative Commons Attribution (CC BY) license (<https://creativecommons.org/licenses/by/4.0/>).

1. Introduction

Recently, electric vehicles (EVs) have garnered significant attention, thanks to their clean and pollution-free operation. However, the widespread adoption of EVs faces several challenges, prominent among which is the charging issue [1]. The ability to charge EVs conveniently and efficiently is crucial for their practicality and widespread acceptance by consumers. To prompt the popularization of EVs, the charging issue has been widely researched [2–4]. Different from traditional geographically fixed charging piles and additionally installed onboard chargers, electric-drive-reconstructed onboard chargers (EDROCs) [5] feed EV batteries by reutilizing the drivetrain components, which offers a unique advantage in terms of cost and power density, providing a novel design concept for an EV charging system.

Multi-phase machines are featured with superior torque performance and outstanding fault tolerance [6], making them well-suited for EVs. Moreover, the distinct characteristic of multi-phase drives, namely the multiple control degrees of freedom [7], can be used to remove the charging torque which is inevitable in a three-phase EDROC implementing fast charging [8]. Currently, EDROC topologies based on multi-phase drive have been extensively investigated [9–12]. A six-phase EDROC employing a three-phase fast charging socket is proposed in [9], which removes the rotating field during charging by rearranging the connection between the three-phase grid and the machine windings. However, the obtained current trajectory of α - β subspace associated with torque generation is line-shaped, which means there is a slight oscillation in this topology. A dot-shaped current path of α - β subspace was achieved in [10] by exploiting the multiple control degrees of

freedom of the six-phase drive, which indicates that the charging torque is always zero at any moment. This significantly increases the reliability of EV charging systems.

At present, the concept of multi-channel charging has emerged in the field of EVs, drawing inspiration from the multi-modular systems utilized in wind power generation [13,14]. The multi-modular system consists of several independent wind turbine modules, wherein each one is capable of operating independently or collectively. If one module fails, the others can still continue to generate power, thus ensuring the reliability and stability of the entire system [15]. Building on this idea, multi-channel charging has been introduced to EVs to improve their reliability and fault tolerance [16,17]. Specifically, for a dual-channel EDROC equipped with a six-phase machine, two batteries are employed on the DC side [18]. One battery, in conjunction with a set of three-phase machine windings, forms one channel, while the other battery, connected to the remaining windings, constitutes the second channel. This dual-channel setup ensures redundancy and fault tolerance, allowing the system to continue working in the event of a channel failure.

However, the difference in voltage levels between the two batteries [19] should be taken into consideration in a dual-channel EDROC. When the voltages of the two batteries are balanced, the system behaves similarly to a single-channel EDROC [20]. If they are unbalanced, a unique operation mode, called the unbalanced charging voltage operation mode, exists in this topology. This leads to different winding currents following through two channels, and further results in a charging torque of the machine, which will be discussed in detail in Section 2. To ensure safe charging, it is necessary to remove the undesired charging torque.

In this article, a dual-channel EDROC incorporating an asymmetrical six-phase permanent magnet synchronous machine (ASPMSM) is studied. The novelty of this paper can be summarized as follows:

1. The operational principles under both the balanced and unbalanced operation modes are analyzed in detail, which indicates that a charging torque is inevitable under the unbalanced charging voltage operation mode, and the following particular conclusion can be reached: balanced winding currents of dual channels are favorable for charging torque elimination.
2. An effective charging torque elimination method based on dual-channel winding current balance is presented, which can ensure a dot-shaped current path in α - β subspace.
3. The controller of the dual-channel EDROC, for both the balanced and unbalanced charging voltage operation modes, is designed. Meanwhile, a prototype of the dual-channel EDROC is built, to verify the effectiveness of the proposed method.

2. Dual-Channel Electric-Drive-Reconstructed Onboard Charger Based on Asymmetrical Six-Phase Permanent Magnet Synchronous Machine

2.1. Topology

A dual-channel EDROC incorporating an ASPMSM is presented in Figure 1. The machine windings A and V are connected to phase a of the grid, winding B, in conjunction with winding W, is with phase b , and windings C and U correspond to phase c . Meanwhile, windings A, B, and C connected to a three-phase voltage source inverter (VSI), to constitute charging channel I, through which the AC input supplies a set of batteries. The remaining windings are connected to the other VSI, forming charging channel II, through which the AC input feeds the other set of batteries.

It should be noted that the ASPMSM is featured with multiple control degrees of freedom. Through vector space decomposition (VSD), the strongly coupled variables in the natural coordinate frame can be injected into three mutually independent subspaces. The specific VSD transformation for the ASPMSM is as follows:

$$\mathbf{T} = \frac{1}{3} \begin{bmatrix} 1 & \cos \delta & \cos 4\delta & \cos 5\delta & \cos 8\delta & \cos 9\delta \\ 0 & \sin \delta & \sin 4\delta & \sin 5\delta & \sin 8\delta & \sin 9\delta \\ 1 & \cos 5\delta & \cos 8\delta & \cos \delta & \cos 4\delta & \cos 9\delta \\ 0 & \sin 5\delta & \sin 8\delta & \sin \delta & \sin 4\delta & \sin 9\delta \\ 1 & 0 & 1 & 0 & 1 & 0 \\ 0 & 1 & 0 & 1 & 0 & 1 \end{bmatrix} \begin{bmatrix} \alpha \\ \beta \\ x \\ y \\ 0_1 \\ 0_2 \end{bmatrix} \quad (1)$$

where δ is equal to $\pi/6$.

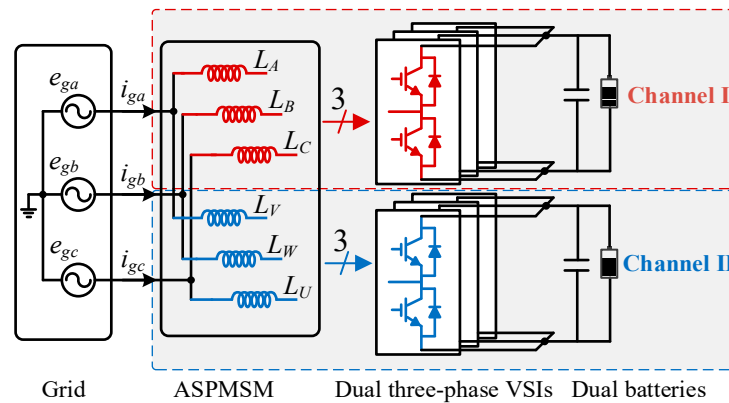


Figure 1. Topology of dual-channel EDROC.

The components of α - β subspace are associated with electromechanical energy conversion, and the components of the x - y and 0_1 - 0_2 subspaces are both unrelated to electromechanical energy conversion, which plays a crucial role in the charging torque elimination.

2.2. Balanced Charging Voltage Operation Mode

The balanced charging voltage operation mode can be implemented by injecting currents into the x - y subspace, while the current components of the α - β and 0_1 - 0_2 subspaces are controlled to zero. In order to satisfy zero charging torque, the currents of three subspaces can be expressed as follows:

$$\begin{cases} i_\alpha = 0 \\ i_\beta = 0 \\ i_x = k \cos(\theta_g - 15^\circ) \\ i_y = k \cos(\theta_g + 75^\circ) \\ i_{01} = 0 \\ i_{02} = 0 \end{cases} \quad (2)$$

where i_α and i_β are the currents of the α - β subspace, i_x and i_y correspond to the x - y subspace, i_{01} and i_{02} relate to the 0_1 - 0_2 subspace, k is the amplitude of i_x and i_y , and θ_g is the phase of the grid.

Using the inverse VSD transformation deduced by Equation (1), the six winding currents of the ASPMSM can be obtained as follows:

$$\begin{cases} i_A = k \cos(\theta_g - 15^\circ) \\ i_B = k \cos(\theta_g - 135^\circ) \\ i_C = k \cos(\theta_g + 105^\circ) \\ i_U = k \cos(\theta_g + 135^\circ) \\ i_V = k \cos(\theta_g + 15^\circ) \\ i_W = k \cos(\theta_g - 105^\circ) \end{cases} \quad (3)$$

Based on the topology shown in Figure 1, the grid-side currents can be acquired as follows:

$$\begin{cases} i_{ga} = i_A + i_V = 2k \cos 15^\circ \cos \theta_g \\ i_{gb} = i_B + i_W = 2k \cos 15^\circ \cos(\theta_g - 120^\circ) \\ i_{gc} = i_C + i_U = 2k \cos 15^\circ \cos(\theta_g - 240^\circ) \end{cases} \quad (4)$$

It is clear that the requirement of grid current balance can be satisfied. Therefore, it is easy to achieve safe charging, in case the winding currents of the dual channels are balanced.

2.3. Unbalanced Charging Voltage Operation Mode

If the charging voltages of the two batteries are unbalanced, the charging power demands of the two channels will be unequal. Further, the winding currents following through the two channels will be unbalanced as well, which can be expressed as follows:

$$\begin{cases} i_A = k_1 \cos(\theta_g - 15^\circ) \\ i_B = k_1 \cos(\omega_g t - 135^\circ) \\ i_C = k_1 \cos(\omega_g t + 105^\circ) \\ i_U = k_2 \cos(\omega_g t + 135^\circ) \\ i_V = k_2 \cos(\omega_g t + 15^\circ) \\ i_W = k_2 \cos(\omega_g t - 105^\circ) \end{cases} \quad (5)$$

where k_1 and k_2 are the winding current amplitudes of two channels, which are determined by the charging voltages.

Assuming that k_1 is 0.5 times as much as k_2 , based on Equation (1), the three subspace currents can be deduced as follows:

$$\begin{cases} i_\alpha = 0.25k_2 \cos(\theta_g + 165^\circ) \\ i_\beta = 0.25k_2 \cos(\theta_g + 75^\circ) \\ i_x = 0.75k_2 \cos(\theta_g - 15^\circ) \\ i_y = 0.75k_2 \cos(\theta_g + 75^\circ) \\ i_{01} = 0 \\ i_{02} = 0 \end{cases} \quad (6)$$

The current trajectory of the α - β subspace associated with torque generation is shown in Figure 2. It can be seen that the current path is an ellipse, indicating a charging torque generation.

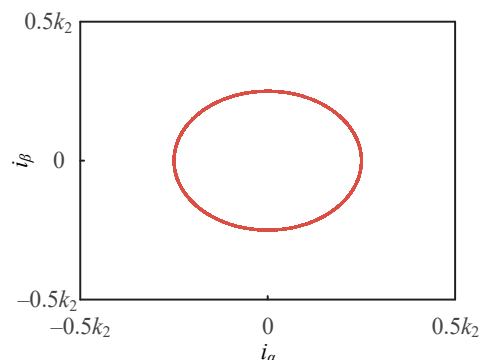


Figure 2. Current trajectories with unbalanced charging voltages.

Moreover, the grid current can be deduced as Equation (7). It is difficult to obtain balanced grid currents.

$$\begin{cases} i_{ga} = i_A + i_V = 0.5k_2 \cos(\theta_g - 15^\circ) + k_2 \cos(\theta_g + 15^\circ) \\ i_{gb} = i_B + i_W = 0.5k_2 \cos(\theta_g - 135^\circ) + k_2 \cos(\theta_g - 105^\circ) \\ i_{gc} = i_C + i_U = 0.5k_2 \cos(\theta_g + 105^\circ) + k_2 \cos(\theta_g + 135^\circ) \end{cases} \quad (7)$$

It can be easily concluded that the charging requirements are hard to satisfy due to the unbalanced dual-channel winding currents under the unbalanced charging voltage operation mode. With reference to the balanced case, if the dual-channel winding currents are balanced, the undesired charging torque is eliminated and the balanced grid currents are obtained.

3. Proposed Effective Charging Torque Elimination Method

In order to simultaneously satisfy the two requirements under the unbalanced charging voltage operation mode, namely the zero charging torque and the balanced grid currents, an effective charging torque elimination method, based on dual-channel winding current balance, is proposed and will be discussed shortly.

To acquire the balanced dual-channel winding currents, the input power requirements of the two channels under the unbalanced charging voltage operation mode should be controlled consistently. The power calculations of one channel are generally expressed as follows:

$$\begin{cases} P_1 = \sum_{j=A,B,C} u_j i_j \cos \varphi_j \\ P_2 = u_{dc} i_{dc} = \frac{u_{dc}^2}{R_{dc}} \\ P_{loss} = P_1 - P_2 \end{cases} \quad (8)$$

where P_1 , P_2 , and P_{loss} denote the input, output, and loss power of one channel, respectively; u_j and i_j denote the input voltage and current for phase j in one channel, separately; φ_j denotes the input power factor of phase j ; u_{dc} and i_{dc} denote the charging voltage and current of the output side, respectively; and R_{dc} is the load resistance.

Assuming that dual channels have the same lost powers, according to Equation (8), to acquire consistent input powers, the output powers must be controlled to the same values.

For simplification, the resistors R_1 and R_2 are used as the dual-channel loads in this paper. In a case where R_1 and R_2 are not equal, the charging voltages should be adjusted correspondingly for the purpose of consistent output powers. The relationship between the dual-channel desired charging voltages is given as follows:

$$\frac{u_{ref1}}{u_{ref2}} = \sqrt{\frac{R_1}{R_2}} \quad (9)$$

It should be added that, for a practical system in which two batteries are used as the dual-channel loads, a combination of different charging modes is required. For constant current charging mode, the charging currents are tuned according to actual charging voltages, and the relationship between dual-channel desired charging currents is expressed as follows:

$$\frac{i_{ref1}}{i_{ref2}} = \frac{u_{dc2}}{u_{dc1}} \quad (10)$$

where u_{dc1} and u_{dc2} are the actual terminal voltages of two batteries, respectively. The constant voltage charging mode is analogous to the resistant load case, where Equation (9) is replaced by the following:

$$\frac{u_{ref1}}{u_{ref2}} = \frac{i_{dc2}}{i_{dc1}} \quad (11)$$

where i_{dc1} and i_{dc2} are the actual charging currents of two channels.

4. Controller Design and Simulations

4.1. Controller Design

The control diagram, which is shared for the balanced and unbalanced charging voltage operation modes, is shown in Figure 3, which consists of a dual-channel winding current balance controller, a voltage outer loop, a phase-locked loop (PLL), a current calculator, a current inner loop, and a pulse width modulation (PWM) generator. The

dual-channel winding current balance controller is responsible for regulating the desired dual-channel charging voltages to balance the winding currents of two channels, so that the generated charging torque can be eliminated under the unbalanced charging voltage operation mode. R_1 and R_2 in Equation (9) are adjustable, according to the actual values. Under the balanced charging voltage operation mode, the ratio R_1/R_2 is set to one.

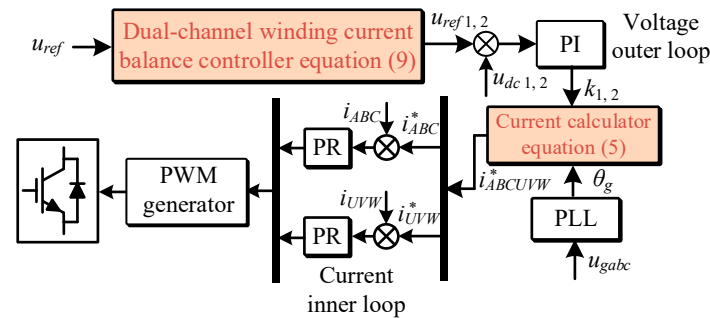


Figure 3. Control diagram (a letter with “*” denotes the reference value).

Next, a proportional integral (PI) controller is employed to regulate the charging voltages, and the amplitudes of the winding currents can be obtained. The values, in conjunction with the grid phase detected by the PLL, are fed into the current calculator. Then, the winding current references which can satisfy the grid current balance and simultaneously achieve unity power factor are obtained.

Subsequently, six proportional resonant (PR) controllers are used in the current inner loop, which make the actual winding currents follow the expected ones. For simplicity, all the machine windings of ASPMSM are assumed to be the same; thus, the parameters of the six PR controllers can be set identically. Even though there are slight differences between windings in the actual system, the desired performance is achieved by only fine-tuning the parameters. Finally, the gating signals of switches are obtained from the PWM generator.

4.2. Simulations

In order to verify the proposed method, simulations are conducted in MATLAB/Simulink. In the simulations, the resistors R_1 and R_2 are used as the dual-channel loads. The switching frequency is set to 10 kHz. The grid voltage is set to 40 V (root mean square value, RMS), and the charging voltage of channel I is determined to be 120 V.

Firstly, the simulation is conducted with $R_1 = 25 \Omega$ and $R_2 = 25 \Omega$, and the results are shown in Figure 4. It can be observed that the balanced grid currents can be obtained under the unity power factor operation, shown in Figure 4a. The winding current i_V leads i_A by approximately 30 degrees in phase, and i_A has the same amplitude as i_V , consistent with Equation (3). The decoupled currents of three subspaces are depicted in Figure 4b. It can be seen that the current path of the α - β subspace is a dot in shape, which indicates there is no charging torque generation. Moreover, the dual-channel charging voltages are shown in Figure 4c. It is clear that the charging voltages are both 120 V, which align with their respective desired values in the steady state, as expected. Also, the dual-channel charging powers maintain balanced, as presented in Figure 4d.

Following this, in order to verify the effectiveness of the proposed method, R_1 and R_2 are adjusted to 25 Ω and 20 Ω , respectively. It should be mentioned that the desired charging voltage of channel II is calculated by Equation (9) for the purpose of charging torque elimination. The simulation results are shown in Figure 5. As presented in Figure 5a, the balanced grid currents and unity power factor operation are achieved; at the same time, i_V is about 30 degrees ahead of i_A in phase with equal amplitude, which is consistent with the case that $R_1 = 25 \Omega$ and $R_2 = 25 \Omega$. Additionally, the current trajectories are depicted in Figure 5b, where the excitation of the α - β subspace is shaped like the original, indicating no charging torque generation. Concurrently, dual-channel charging voltage and power values are shown in Figures 5c and 5d, respectively. Notably, the actual charging voltages

accurately follow their setpoints while maintaining balanced dual-channel power values, which exhibit the same steady performance as the case where $R_1 = 25 \Omega$ and $R_2 = 25 \Omega$.

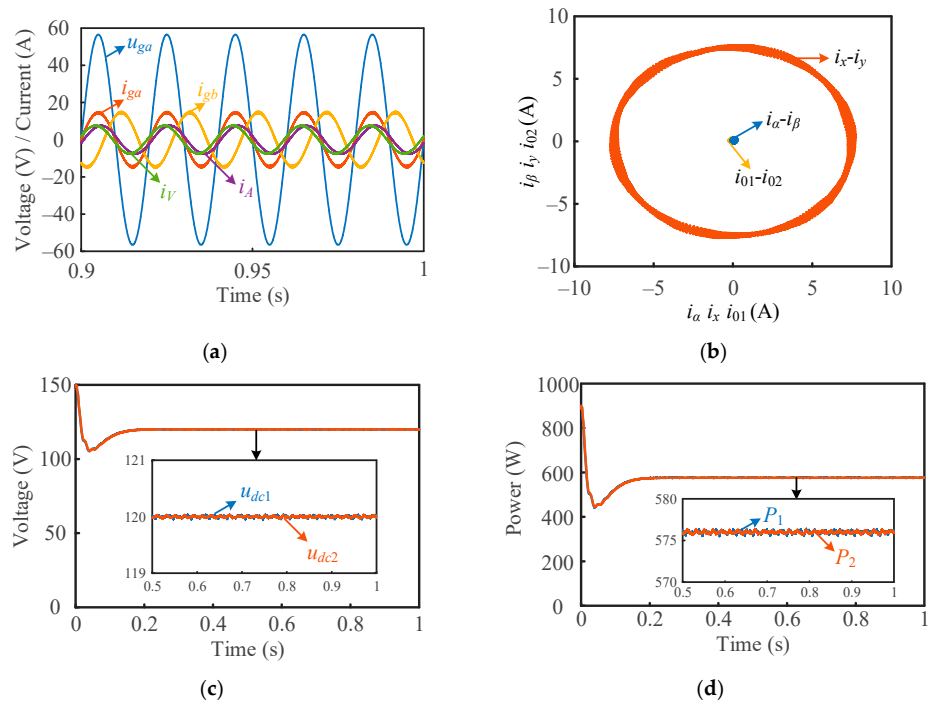


Figure 4. $R_1 = 25 \Omega$ and $R_2 = 25 \Omega$. (a) Grid voltage of phase a , grid currents of phase a and b , and winding currents of phase A and V ; (b) current trajectories of three subspaces; (c) dual-channel charging voltages; (d) dual-channel charging power values.

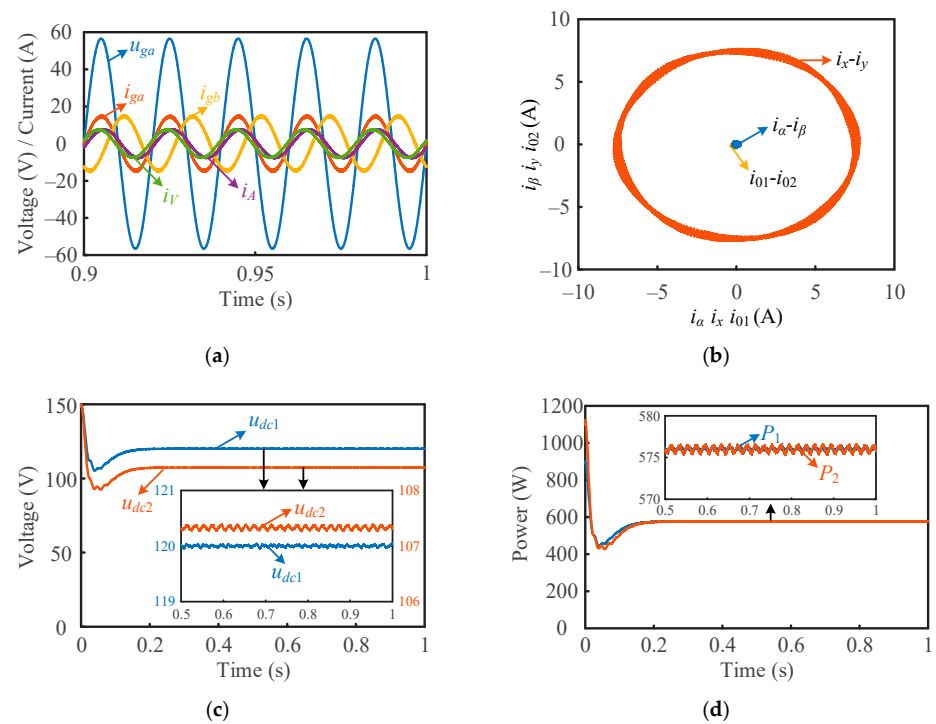


Figure 5. $R_1 = 25 \Omega$ and $R_2 = 20 \Omega$. (a) Grid voltage of phase a , grid currents of phase a and b , and winding currents of phase A and V ; (b) current trajectories of three subspaces; (c) dual-channel charging voltages; (d) dual-channel charging power values.

Finally, R_1 and R_2 are determined as 25Ω and 30Ω , and the results are displayed in Figure 6. It is evident that balanced grid currents are obtained under the unity power factor operation from Figure 6a. Also, i_A and i_V show similar characteristics as those in the aforementioned cases. Meanwhile, the current trajectory of the α - β subspace is dot-shaped, as presented in Figure 6b, indicating no charging torque generation. Figure 6c,d provide dual-channel charging voltage and power values, respectively, which are similar to the two cases above.

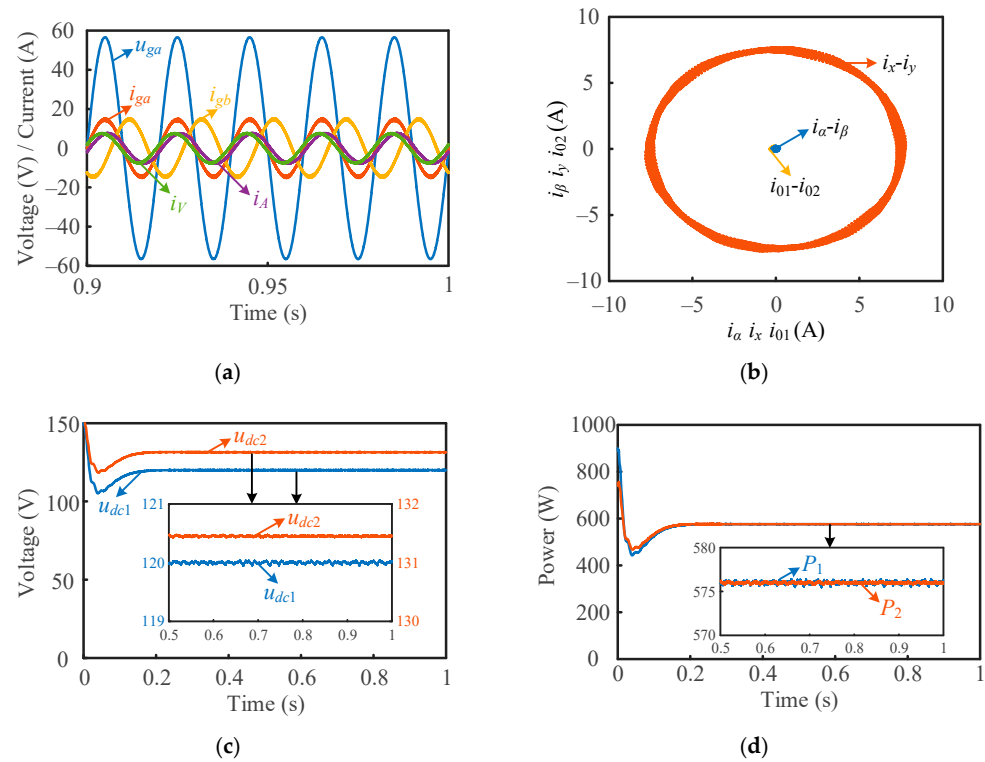


Figure 6. $R_1 = 25 \Omega$ and $R_2 = 30 \Omega$. (a) Grid voltage of phase a , grid currents of phase a and b , and winding currents of phase A and V ; (b) current trajectories of three subspaces; (c) dual-channel charging voltages; (d) dual-channel charging power values.

5. Experiments

In order to verify the proposed charging torque elimination method, a dual-channel EDROC prototype is built. As shown in Figure 7, the experimental rig consists of a three-phase power source, an ASPMSM, dual three-phase VSIs, and two loads. It should be mentioned that the three-phase power source is used to emulate the three-phase grid. The primary parameters of the tested ASPMSM are displayed in Table 1. Meanwhile, the dual three-phase VSIs comprise six Infineon FF300R12ME4 modules. Due to the limitations of the experimental equipment and for the purpose of safety, an adjustable resistor bank and a programmable electronic load are employed as the dual-channel loads, respectively. The different loads make no difference to the experimental results, because the resistor values are both adjustable. In addition, the system necessitates six WHB25LSP3S1 current sensors for capturing the winding currents, along with four WHV05AS3S6 voltage sensors for sampling the two-phase grid voltages and dual-channel charging voltages. A TI TMS320F28335 digital signal processor, programmed with control code written in C, is used to process all the sensed signals and execute real-time control tasks.

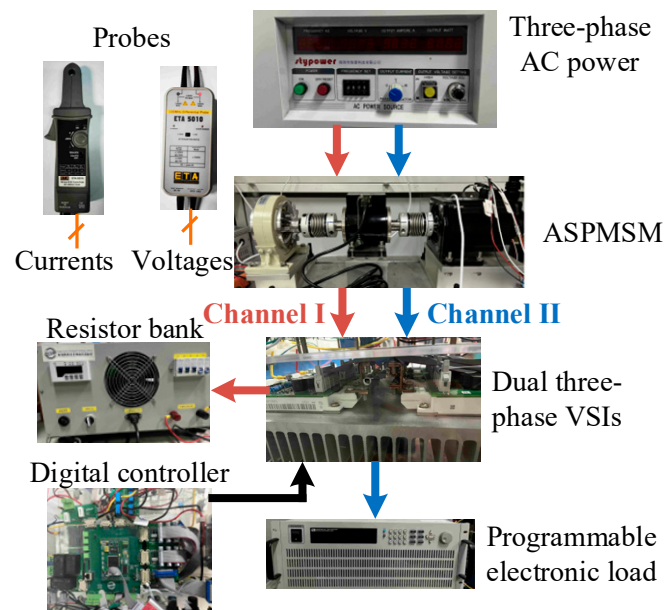


Figure 7. Experimental rig.

Table 1. Main parameters of the tested ASPMSM.

Parameters	Values
Rated power	2 kW
Rated voltage	220 V
Rated current	12 A
Number of pole pairs	5
Direct axis inductance	6.18 mH
Quadrature axis inductance	6.13 mH
Stator resistance	0.7 Ω
Stator leakage inductance	1.82 mH

Experiments are conducted under three different dual-channel load resistance ratio (R_1/R_2) conditions, and the grid voltage is always set to 40 V (RMS). In addition, the sampling frequency is set as 10 kHz.

Firstly, the dual-channel EDROC is tested under the balanced charging voltage operation mode with $R_1 = 25 \Omega$ and $R_2 = 25 \Omega$. The dual-channel charging voltages are both set to 120 V, and the results are shown in Figure 8. As shown in Figure 8a, the balanced grid currents are achieved. The grid voltage and current of phase a are in phase, indicating that the unity power factor operation is realized. It can be seen from Figure 8b that the winding current, i_V , is about 30 degrees ahead of i_A in phase and i_A has the same amplitude as i_V , which is in accordance with Equation (3). In addition, the total harmonic distortion (THD) of grid current i_{ga} is about 1.05%, as shown in Figure 8c. The current trajectories of three subspaces are depicted in Figure 8d, where the current path in the α - β subspace is approximated to an origin, indicating no charging torque generation. Meanwhile, the active power values (P_1 and P_2) and the charging voltages (u_{dc1} and u_{dc2}) of two channels are presented in Figure 8e,f. From Figure 8e, it is clear that the dual-channel power values are balanced, and the charging voltages are expected to track their individual desired values in the steady state. Figure 8f shows the dynamic performance. During the charging voltage changing from 120 V to 130 V, a smooth curve is obtained, and the response process, roughly, lasts for 100 ms. The actual dual-channel charging voltages can both accurately follow their setpoints, and the dual-channel power values always maintain balanced.

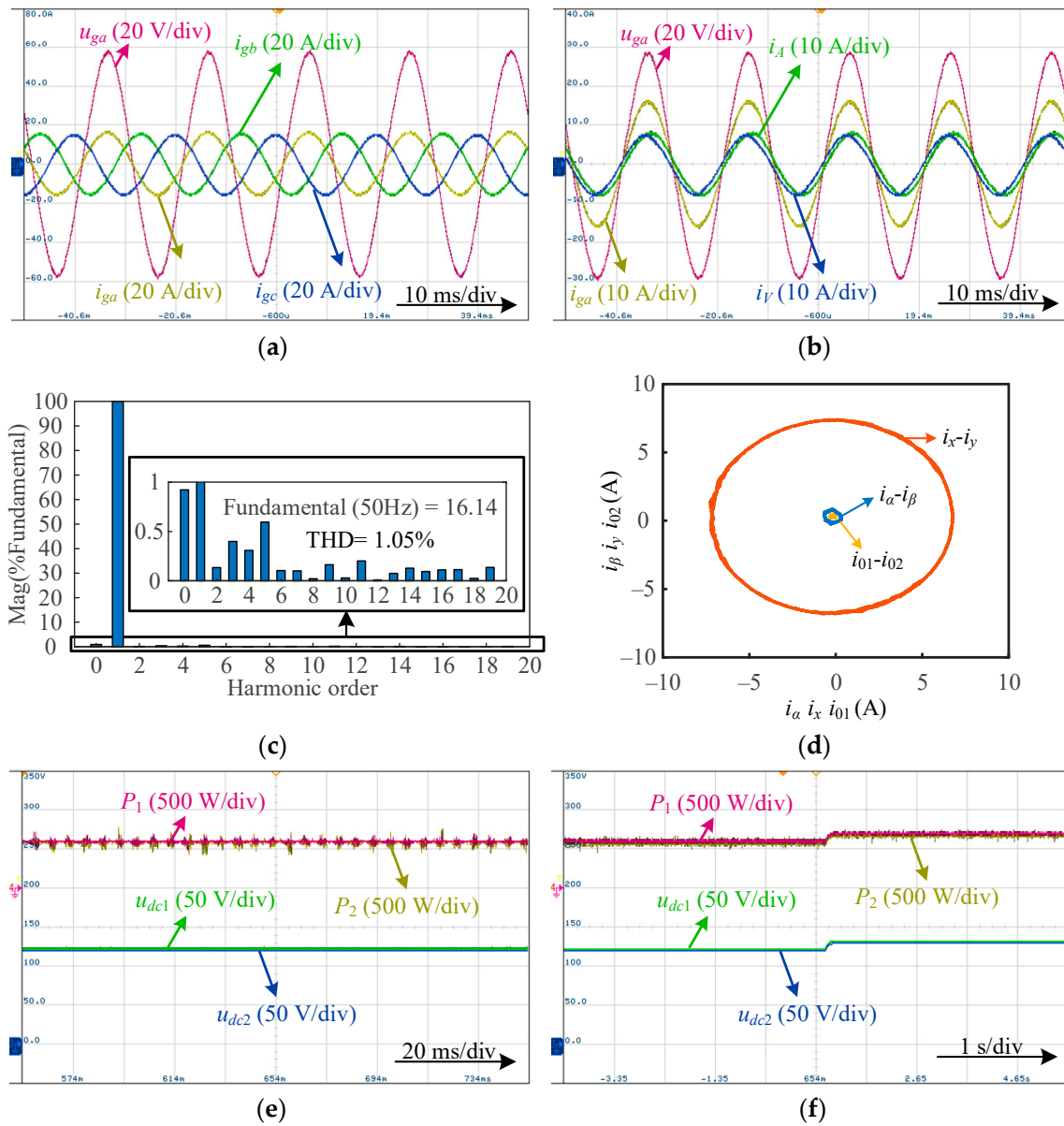


Figure 8. Balanced charging voltage operation mode, with $R_1 = 25 \Omega$ and $R_2 = 25 \Omega$. (a) Grid voltage of phase a and grid currents; (b) grid voltage and current of phase a and winding currents of phase A and V ; (c) grid current THD of phase a ; (d) current trajectories of three subspaces; (e) steady performance; (f) dynamic performance.

Subsequently, the experiment is conducted under the unbalanced charging voltage operation mode, with $R_1 = 25 \Omega$ and $R_2 = 20 \Omega$. The charging voltage of channel I is set to 125 V. In order to eliminate the charging torque discussed in Section 2.3, the charging voltage of channel II is calculated using Equation (9). The results are shown in Figure 9. The balanced grid currents and the unity power factor operation are realized as in Figure 9a. Similar to the balanced charging voltage operation mode, i_V is about 30 degrees ahead of i_A in phase and i_A has the same amplitude as i_V , as presented in Figure 9b. Additionally, the grid current i_{ga} follows a THD of about 1.02%, as shown in Figure 9c. The decoupled current trajectories are drawn in Figure 9d. It can be seen that the current trajectory in the α - β subspace is a proximate origin in shape, which means there is no charging torque generation. At the same time, Figure 9e,f present the active power values (P_1 and P_2) and the charging voltages (u_{dc1} and u_{dc2}) of two channels. Notably, the dual-channel power values remain balanced, and the charging voltages precisely track their respective desired

values during the steady-state operation mode, as shown in Figure 9e. Figure 9f depicts the dynamic performance, where the transition from a 120 V to a 130 V charging voltage exhibits a smooth curve, with a response time of approximately 100 ms. Throughout the process, the actual dual-channel charging voltages accurately follow their setpoints, while maintaining balanced dual-channel power values.

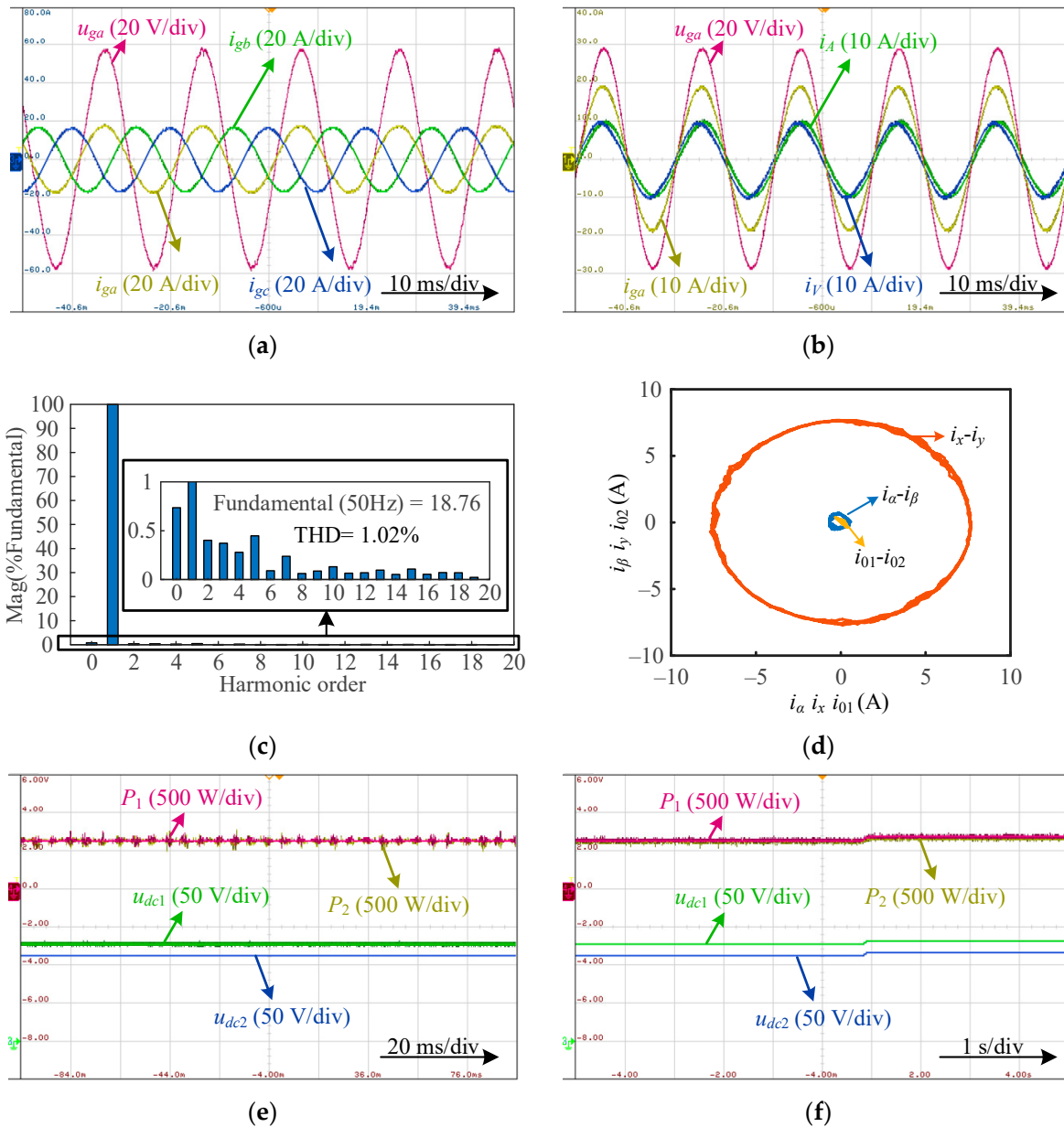


Figure 9. Unbalanced charging voltage operation mode, with $R_1 = 25 \Omega$ and $R_2 = 20 \Omega$. (a) Grid voltage of phase a and grid currents; (b) grid voltage and current of phase a and winding currents of phase A and V; (c) grid current THD of phase a; (d) current trajectories of three subspaces; (e) steady performance; (f) dynamic performance.

Ultimately, R_1 and R_2 are adjusted to 25Ω and 30Ω , separately. The results are shown in Figure 10. It is clear that balanced grid currents are obtained under the unity power factor operation, as shown in Figure 10a. The currents i_{ga} , i_A , and i_V are provided in Figure 10b. It can be seen that i_V is about 30 degrees ahead of i_A in phase and i_A has the same amplitude as i_V , which is the same as the aforementioned two cases. Also, i_{ga} has a THD of about 1.15%, as shown in Figure 10c. Meanwhile, the current trajectories of three subspaces are

presented in Figure 10d. The excitation of the α - β subspace is a dot, indicating there is no charging torque generation. Figure 10e provides the steady performance and Figure 10f gives the dynamic performance when the charging voltage of channel I is changed from 120 V to 130 V, which are similar to the two cases above and will be not repeated here.

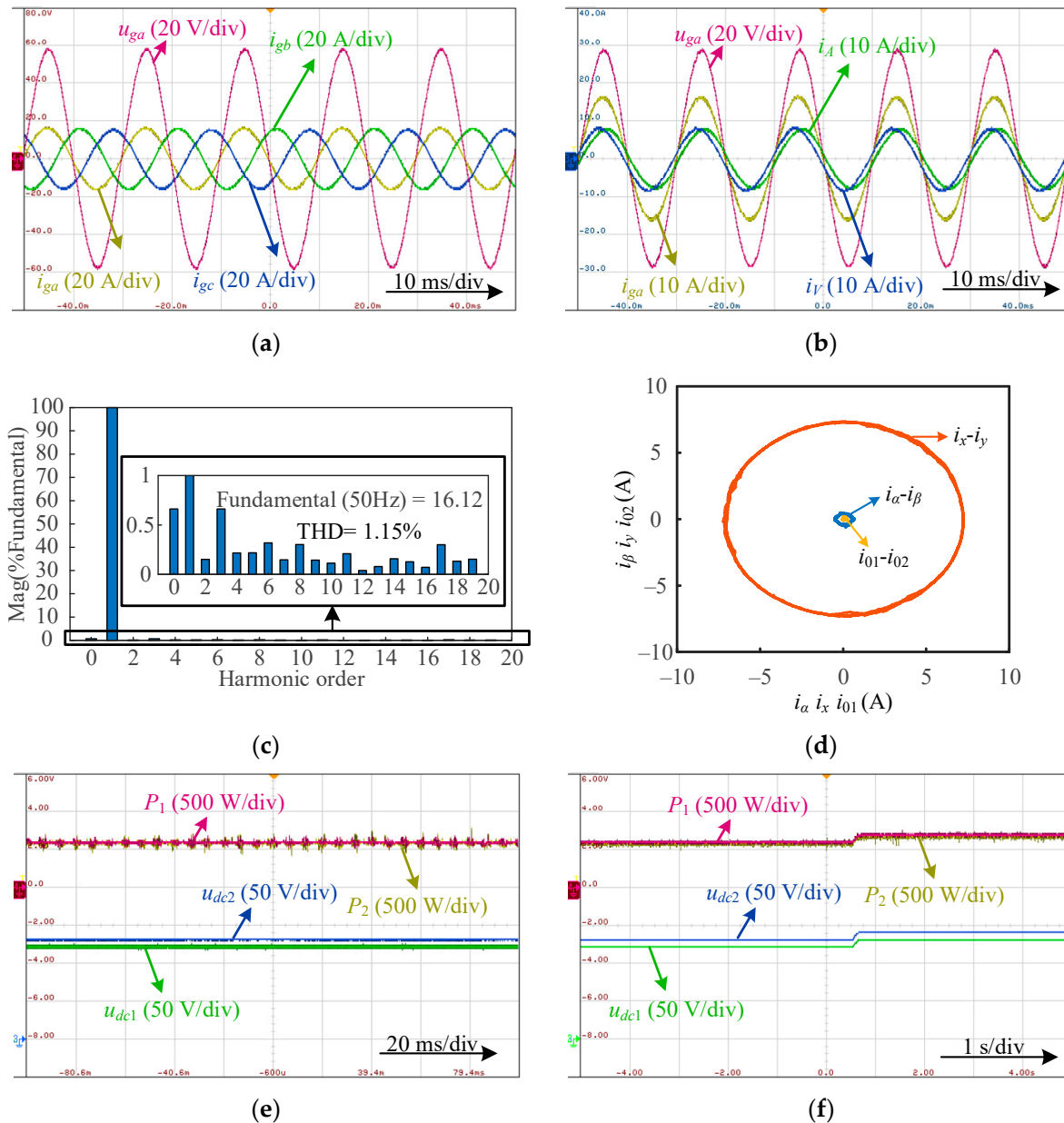


Figure 10. Unbalanced charging voltage operation mode, with $R_1 = 25 \Omega$ and $R_2 = 30 \Omega$. (a) Grid voltage of phase a and grid currents; (b) grid voltage and current of phase a and winding currents of phase A and V ; (c) grid current THD of phase a ; (d) current trajectories of three subspaces; (e) steady performance; (f) dynamic performance.

In summary, zero charging torque generation can always be realized by using the proposed charging torque elimination method, regardless of whether the dual-channel charging voltages are balanced or unbalanced.

6. Conclusions

This paper studied a dual-channel EDROC topology integrated with an ASPMSM. The balanced and unbalanced charging voltage operation modes of the dual-channel

EDROC are both analyzed. Based on VSD, the current trajectory of the α - β subspace is depicted under the unbalanced charging voltage operation mode, revealing the presence of a charging torque in the ASPMSM. It is proven that unbalanced dual-channel winding currents result in an inevitable charging torque. Subsequently, an effective charging torque elimination method, based on dual-channel winding current balance, is proposed. It can realize balanced winding currents under the unbalanced charging voltage operation mode by making the charging power requirement of two channels consistent, so that zero charging torque is achieved. Finally, experiments are conducted under three different dual-channel load resistance ratio conditions and all of them feature dot-shaped current trajectories on the α - β subspace, which demonstrate that zero charging torque is achieved. The effectiveness of the proposed method in terms of charging torque elimination is further verified.

Author Contributions: Conceptualization, F.Y. and X.C.; methodology, F.Y.; software, X.C.; validation, X.C. and L.Q.; formal analysis, X.C.; investigation, L.Q.; resources, F.Y.; data curation, X.C.; writing—original draft preparation, X.C.; writing—review and editing, F.Y.; visualization, L.Q.; supervision, L.Q.; project administration, F.Y.; funding acquisition, F.Y. All authors have read and agreed to the published version of the manuscript.

Funding: This research was funded by the National Natural Science Foundation of China, grant number 52177051.

Data Availability Statement: The original contributions presented in the study are included in the article, further inquiries can be directed to the corresponding author.

Conflicts of Interest: The authors declare no conflicts of interest.

References

1. Yao, M.; Da, D.; Lu, X.; Wang, Y. A review of capacity allocation and control strategies for electric vehicle charging stations with integrated photovoltaic and energy storage systems. *World Electr. Veh. J.* **2024**, *15*, 101. [[CrossRef](#)]
2. Bernal-Vargas, J.; Castro-Galeano, J.; Tibaduiza-Rincón, E.; López-Lezama, J.; Muñoz-Galeano, N. Prospective analysis of massive integration of electric vehicle chargers and their impact on power quality in distribution networks. *World Electr. Veh. J.* **2023**, *14*, 324. [[CrossRef](#)]
3. Gopalasami, R.; Chokkalingam, B. A photovoltaic-powered modified multiport converter for an EV charger with bidirectional and grid connected capability assist PV2V, G2V, and V2G. *World Electr. Veh. J.* **2024**, *15*, 31. [[CrossRef](#)]
4. Althurthi, S.; Rajashekara, K.; Debnath, T. Comparison of EV fast charging protocols and impact of sinusoidal half-wave fast charging methods on lithium-ion cells. *World Electr. Veh. J.* **2024**, *15*, 54. [[CrossRef](#)]
5. Yu, F.; Zhu, Z.; Liu, X.; Zhang, Z. Electric-drive-reconstructed onboard charger for solar-powered electric vehicles incorporating six-phase machine. *IEEE Trans. Power Electron.* **2022**, *37*, 6544–6555. [[CrossRef](#)]
6. Verkroost, L.; De Belie, F.; Sergeant, P.; Vansompel, H. Multiagent control in modular motor drives by means of deterministic consensus. *IEEE Trans. Ind. Electron.* **2023**, *70*, 1205–1215. [[CrossRef](#)]
7. Munim, W.N.W.A.; Duran, M.J.; Che, H.S.; Bermúdez, M.; González-Prieto, I.; Rahim, N.A. A unified analysis of the fault tolerance capability in six-phase induction motor drives. *IEEE Trans. Power Electron.* **2017**, *32*, 7824–7836. [[CrossRef](#)]
8. Sharma, S.; Aware, M.V.; Bhowate, A. Integrated battery charger for EV by using three-phase induction motor stator windings as filter. *IEEE Trans. Transport. Electrification.* **2020**, *6*, 83–94. [[CrossRef](#)]
9. Liu, X.; Yu, F.; Mao, J.; Yang, H. Pre- and post-fault operations of six-phase electric-drive-reconstructed onboard charger for electric vehicles. *IEEE Trans. Transport. Electrification.* **2022**, *8*, 1981–1993. [[CrossRef](#)]
10. Habib, A.; Shawier, A.; Abdel-Majeed, M.S.; Abdel-Khalik, A.S.; Hamad, M.S.; Hamdy, R.A.; Ahmed, S. Predictive current control of six-phase IM-based nonisolated integrated on-board battery charger under different winding configurations. *IEEE Trans. Power Electron.* **2022**, *37*, 8345–8358. [[CrossRef](#)]
11. Subotic, I.; Bodo, N.; Levi, E. Integration of six-phase EV drivetrains into battery charging process with direct grid connection. *IEEE Trans. Energy Convers.* **2017**, *32*, 1012–1022. [[CrossRef](#)]
12. Tong, M.; Cheng, M.; Wang, S.; Hua, W. An on-board two-stage integrated fast battery charger for EVs based on a five-phase hybrid-excitation flux-switching machine. *IEEE Trans. Ind. Electron.* **2021**, *68*, 1780–1790. [[CrossRef](#)]
13. Subotic, I.; Dordevi, O.; Gomm, J.B.; Levi, E. Active and reactive power sharing between three-phase winding sets of a multiphase induction machine. *IEEE Trans. Energy Convers.* **2019**, *34*, 1401–1410. [[CrossRef](#)]
14. Zoric, I.; Jones, M.; Levi, E. Arbitrary power sharing among three-phase winding sets of multiphase machines. *IEEE Trans. Ind. Electron.* **2018**, *65*, 1128–1139. [[CrossRef](#)]
15. Yan, L.; Zhu, Z.Q.; Qi, J.; Ren, Y.; Gan, C.; Brockway, S.; Hilton, C. Suppression of major current harmonics for dual three-phase PMSMs by virtual multi three-phase systems. *IEEE Trans. Ind. Electron.* **2022**, *69*, 5478–5490. [[CrossRef](#)]

16. Viana, C.; Pathmanathan, M.; Lehn, P.W. Dual-inverter-integrated three-phase EV charger based on split-phase machine. *IEEE Trans. Power Electron.* **2022**, *37*, 15175–15185. [[CrossRef](#)]
17. Wang, Z.; Liu, B.; Guan, L.; Zhang, Y.; Cheng, M.; Zhang, B.; Xu, L. A dual-channel magnetically integrated EV chargers based on double-stator-winding permanent-magnet synchronous machines. *IEEE Trans. Ind. Appl.* **2019**, *55*, 1941–1953. [[CrossRef](#)]
18. Yu, F.; Wang, Z.; Wang, Y.; Zhou, C. Decoupled and compensated space vector pulse width modulation algorithm for dual-channel PMSM with unbalanced power supplies. *Int. J. Circ. Theor. Appl.* **2024**, *52*, 1813–1829. [[CrossRef](#)]
19. Liao, W.; Lyu, M.; Huang, S.; Wen, Y.; Li, M.; Huang, S. An enhanced SVPWM strategy based on vector space decomposition for dual three phase machines fed by two DC-source VSIs. *IEEE Trans. Power Electron.* **2021**, *36*, 9312–9321. [[CrossRef](#)]
20. Raherimihaja, H.J.; Zhang, Q.; Na, T.; Shao, M.; Wang, J. A three-phase integrated battery charger for EVs based on six-phase open-end winding machine. *IEEE Trans. Power Electron.* **2020**, *35*, 12122–12132. [[CrossRef](#)]

Disclaimer/Publisher’s Note: The statements, opinions and data contained in all publications are solely those of the individual author(s) and contributor(s) and not of MDPI and/or the editor(s). MDPI and/or the editor(s) disclaim responsibility for any injury to people or property resulting from any ideas, methods, instructions or products referred to in the content.